ISDE   **AIR**   **Taylor & Francis**
Taylor & Francis Group

Synergic sensing of light and heat emitted by offshore oil and gas platforms in the South China Sea

Yujia Qiu [a,e,f], Xiao-Ming Li [b,c,d], Lin Yan [a,e] and Zhongzhong Chen[a,e,g]

[a]Key Laboratory of Digital Earth Science, Aerospace Information Research Institute, Chinese Academy of Sciences, Beijing, People's Republic of China; [b]Hainan Aerospace Technology Innovation Center, Wenchang, People's Republic of China; [c]Key Laboratory of Earth Observation of Hainan Province, Hainan Aerospace Information Research Institute, Wenchang, People's Republic of China; [d]School of Computer and Information Engineering, Henan University, Kaifeng, People's Republic of China; [e]International Research Center of Big Data for Sustainable Development Goals, Beijing, People's Republic of China; [f]University of Chinese Academy of Sciences, Beijing, People's Republic of China; [g]College of Geomatics and Geoinformation, Guilin University of Technology, Guilin, People's Republic of China

ABSTRACT

Facing the growing global demand for oil resources and the industry's commitment to decarbonization, there is a need for customized monitoring of oil and gas (OG) platforms. Remote sensing has proved an effective approach for OG platform observation compared to in-situ surveys. However, coarse spatial resolution and unbefitting spectra confine the application in monitoring platform activities. The Sustainable Development Science Satellite 1 (SDGSAT-1) has a comprehensive advantage, providing high spatial resolution (up to 10 m) and wide swath (300 km) imaging capability while enabling synchronous observation of the Glimmer Imager (GLI) and Thermal Infrared Spectrometer (TIS) at night. In this study, we demonstrated for the first time the synergic application of the SDGSAT-1 GLI and TIS to observe offshore OG platforms, probing their peculiar activities of associated gas flaring. By incorporating GLI visible colour bands, we developed an algorithm for gas flaring detection, pinpointing 113 active OG platforms in the South China Sea. The SDGSAT-1 not only pinpoints the offshore OG platforms but also provides insights into understanding their light- and heat-emitting variations. These findings highlight the competence of SDGSAT-1 in tracking the operational status of OG platforms and contributing to further refining the OG platform inventory.

1. Introduction

Meeting the growing global energy demands while advancing energy decarbonization presents a significant challenge shared worldwide (AlixPartners 2022; GGRP 2021). Offshore oil and gas (OG) platforms are crucial facilities for extracting and processing crude oil and natural gas. However, their remote ocean locations make it impractical to transport all extracted crude oil and natural gas via pipeline distribution systems to inland markets. As a result, offshore OG platforms often flare the associated natural gas due to safety and economic considerations. Unfortunately, gas

flaring contributes to air pollution and greenhouse gas emissions (Fawole, Cai, and MacKenzie 2016; Ma et al. 2022; Shelestov et al. 2020). Therefore, understanding the location and operation of offshore OG platforms is vital, whether to improve resource efficiency or reduce carbon emissions and protect the environment (Gao, Guan, and Zhang 2022; Mansoor and Tahir 2021).

Satellite remote sensing provides a cost-effective and efficient observation technique, enabling high-resolution, long-term monitoring over vast areas without direct access (UNCTAD 2021; Yang et al. 2013), serving as a crucial tool for overseeing offshore OG platform activities. Nighttime light remote sensing, which detects intensified visible and near-infrared radiation signals within a panchromatic band (Pan band) centred at 0.7 μm, has proven effective in depicting artificial lights (Levin et al. 2020). This includes the use of the Defense Meteorological Program (DMSP) Operational LineScan System (OLS) (Elvidge et al. 2009; Sun et al. 2020) and the Visible Infrared Imaging Radiometer Suite (VIIRS) Day-Night Band (DNB) (Chakraborty et al. 2023; Elvidge et al. 2009; Ma et al. 2023; Wang et al. 2021). Given that gas flaring typically occurs at temperatures exceeding 1450 K, resulting in its peak radiation shifting to the short- and mid-infrared regions, multiple spectral channels have been employed to quantify the gas volumes and emissions (Faruolo et al. 2021). A decade-plus history of datasets on flaring gas has been compiled using synthetic multi-year satellite products (Anejionu 2019) from the Along-Track Scanning Radiometer (ATSR) (Casadio, Arino, and Serpe 2012; Fisher and Wooster 2019), the Landsat series (Anejionu, Blackburn, and Whyatt 2014; Schroeder et al. 2016), Moderate Resolution Imaging Spectroradiometer (MODIS) (Anejionu, Blackburn, and Whyatt 2015; Giglio, Schroeder, and Justice 2016), VIIRS (Csiszar et al. 2014; Elvidge et al. 2016; Schroeder et al. 2014; Zhizhin et al. 2021), and the Sentinel-2 Multi-spectral Instrument (MSI) (Liu et al. 2021; 2023).

Nevertheless, a gap remains between current satellite observations and the practical needs of the OG industry. The primary challenge lies in the spatial resolution limitations of available spaceborne sensors, which only provide imaging capability at a moderate resolution (hundreds of metres). In such moderate-resolution data, flares appear as sub-pixel phenomena (Elvidge et al. 2013), making them less effective for small-scale or closely spaced offshore OG platforms. Additionally, the spectral limitations of these sensors hinder the effective monitoring of flaring activities. Synthetic Aperture Radar (SAR) focuses on the morphology of OG platforms (Falqueto et al. 2019; Wong, Thomas, and Halpin 2019) rather than distinguishing between different facilities. Multi-spectral images are susceptible to solar-induced confounding effects, in addition to being confined to a narrow data width to balance its size, e.g. Sentinel-2 MSI (Liu et al. 2021; 2023).

The Sustainable Development Science Satellite 1 (SDGSAT-1), customized for implementing the United Nations 2030 Agenda for Sustainable Development Goals (SDG), offers a unique opportunity for comprehensive detection of offshore OG platforms. Equipped with three sensors of the Glimmer Imager (GLI), the Thermal Infrared Spectrometer (TIS), and the Multi-Spectral Imager (MII), SDGSAT-1 collects high-quality data, enabling the assessment of SDGs (Guo et al. 2023). A significant advantage of SDGSAT-1 is its improved spatial resolution of up to 10 m in parallel with a wide swath of 300 km (Hu et al. 2024). Moreover, the nighttime synchronous observation of the GLI and TIS sensors enhances their application by providing high-resolution light and heat radiation data, free from solar-irradiation effects.

This study introduces a pioneering approach by synergically applying the GLI and TIS sensors onboard SDGSAT-1 to sense light and heat radiation from offshore OG platforms. The overall concept is illustrated in Figure 1. By leveraging the advanced capabilities of SDGSAT-1, we can achieve detailed and extensive observations of offshore OG platforms. Particularly in major oil-producing regions, the GLI's nighttime colour composites effectively reveal the signals from offshore OG platforms during the night, along with visible flames resulting from associated gas flaring (Figure 1(c–f)). Focusing on the South China Sea (SCS), we conducted a thorough analysis of the light and heat radiation from offshore OG platforms, examining their variations and cross-validating with previous gas flaring inventories. This study demonstrates the feasibility of applying the SDGSAT-1 satellite for offshore OG platform detection while exploring associated challenges. The results will support the global OG platform survey
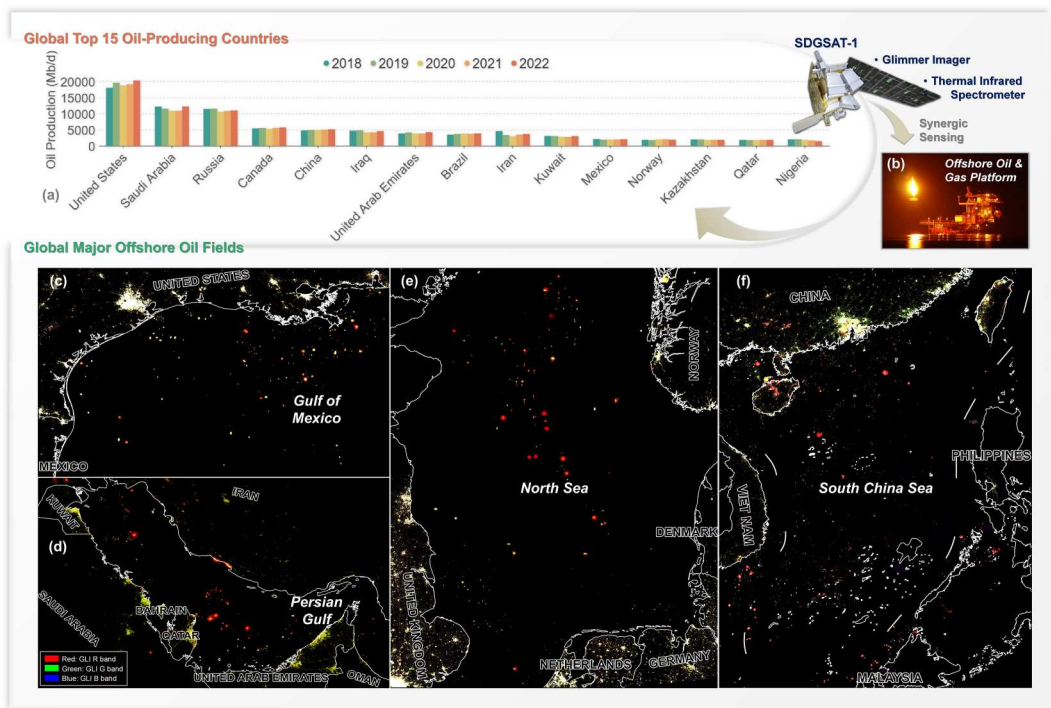
Figure 1. Overview of the study concept for sensing offshore OG platforms using SDGSAT-1. (a) Global oil production of major oil-producing countries from 2018 to 2022 (source: U.S. Energy Information Administration, unit Md/d: thousand barrels per day). (b) The nighttime synchronous capability of SDGSAT-1 GLI and TIS sensors effectively captures details of offshore OG platforms. (c)–(f) SDGSAT-1 GLI nighttime colour composites (GLI R, G, and B band data stretched into 8-bit images and used for three channels) for major offshore oil fields in the Gulf of Mexico, Persian Gulf, North Sea, and SCS, respectively (annual composite results mosaicked from available GLI data in 2022).

in line with SDG 13 (Climate Action) and SDG 14 (Life Below Water) (UN 2015) as well as the initiative to achieve Zero Regular Flaring (ZRF) by 2030 (GGRP 2021).

2. Materials and methods

2.1. Materials

2.1.1. SDGSAT-1 GLI data and TIS data

The SDGSAT-1 crossed the SCS approximately at 21:30 local time. The GLI and the TIS sensors operate synchronously during nighttime, with their key technical specifications outlined in Table 1 (Guo et al. 2023). The GLI sensor achieves a resolution of up to 10 m in its Pan band and features an innovative design with three visible colour bands, i.e. red (R), green (G), and

Table 1. Technical specifications of SDGSAT-1.

	Glimmer imager (GLI)	Thermal infrared spectrometer (TIS)
Spectral Band	Pan: 450–900 nm B: 430–520 nm G: 520–615 nm R: 615–690 nm	B1: 8.0–10.5 μm B2: 10.3–11.3 μm B3: 11.5–12.5 μm
Spatial Resolution	Pan: 10 m B/G/R: 40 m	30 m
Swath Width	300 km	300 km
Designed radiometric accuracy	Relative: ≤ 2% Absolute: ≤ 5%	Relative: ≤ 5% Absolute: ≤ 1 K @ 300 K
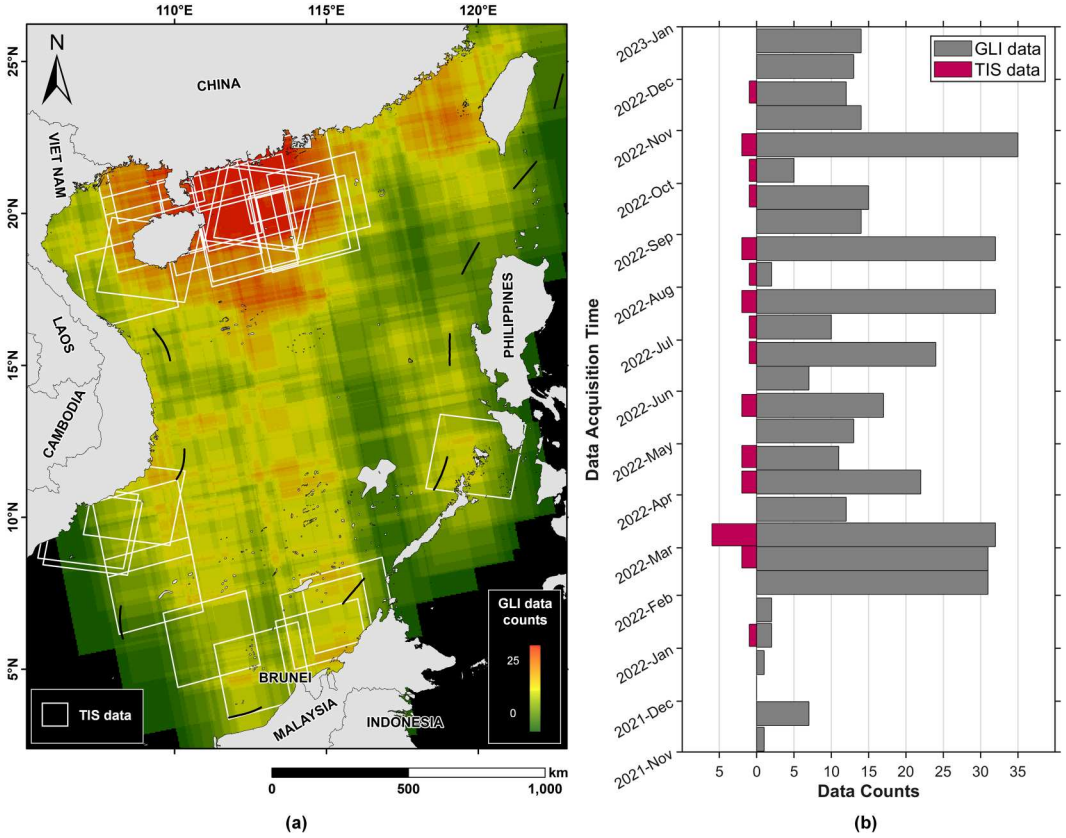
Figure 2. SDGSAT-1 GLI and TIS data collected in the SCS, 2021–2022. (a) Spatial distribution of the SDGSAT-1 data, where the shading colours indicate the coverage of GLI data counts, and the white squares mark the borders of TIS data. (b) Temporal distribution of GLI and TIS data, where the length of each bar represents the number of image scenes acquired over a half-month period.

blue (B) at 40 m resolutions (Yan et al. 2024). A total of 411 GLI images from the SCS were utilized for OG platform detection in this study as shown in Figure 2(a), with acquisition dates spanning from November 2021 to December 2022, illustrated in Figure 2(b). The GLI Pan-band and RGB-bands data were converted to radiance values (units: nW/cm^2/sr/μm) from the digital numbers (DNs) using Equation (1), where *Gain* and *Bias* are provided in the data metafile.

$$L = (Gain \times DN + Bias) \times 10^5 \tag{1}$$

The TIS sensor onboard SDGSAT-1 has three bands, centred respectively at 9.3 μm (band 1, B1), 10.8 μm (band 2, B2), and 11.8 μm (band 3, B3), providing a spatial resolution of 30 m across a wide swath of 300 km and exhibiting good radiometric performance (Hu et al. 2023). 27 TIS images were selected for this study, with the data coverage indicated by the white borders in Figure 2(a), and the temporal distribution illustrated in Figure 2(b). The TIS three-band data were calibrated (using Equation (1)) and converted to bright temperatures using Planck's formula.

Since the real-time cloud product for SDGSAT-1 is not yet available, we utilized the MODIS cloud mask product (Ackerman, Menzel, and Frey 2015) to exclude the GLI and TIS images affected by cloud cover exceeding 60% in combination with manual visual screening. This manual screening is especially important for thermal infrared data, due to the significant cloud contamination and atmospheric interferences, resulting in the removal of many contaminated TIS data in this study.

2.1.2. Reference datasets

We used a collection of high-resolution satellite observations as reference datasets. This includes GF2 visible data (Pan band, 0.45–0.90 μm) at 1 m resolution and Sentinel-1 Interferometric Wide Swath (IW) images in HH polarization, which has a pixel size of 10 m.

Liu et al. (2023) developed a gas flaring detection method based on Sentinel-2 MSI, leveraging two short-wave infrared bands (bands 11 and 12, centred at 1.60 and 2.20 μm) and one near-infrared band (band 8a, centred at 0.865 μm) at 20 m resolution to detect gas flares. They refined their results by accumulating time-series MSI images and compiling an inventory of global offshore gas flaring using approximately 8.53 million offshore Sentinel-2A/2B MSI images from 2015 to 2021. We utilized this inventory (Liu et al. 2023) for comparative analysis.

Additionally, we also used the VIIRS active fire product (NASA FIRMS 2024; Schroeder et al. 2014) and the VIIRS nightfire product (Elvidge et al. 2013; 2016; Zhizhin et al. 2021) for cross-validation. The VIIRS products provide the global mapping of hotspot events, from which we collected the relevant data for 2022 in the SCS.

2.2 Method of detecting offshore OG platforms by SDGSAT-1 GLI

Based on multi-temporal SDGSAT-1 GLI data, we proposed an algorithm for detecting offshore OG platforms. The algorithm, illustrated in Figure 3, consists of two stages. In the first stage, the Pan band images are utilized to segment light-emitting targets in single-phase data and assess their light-emitting frequencies by accumulating multi-temporal images to identify platform candidates with invariant locations. In the second stage, GLI RGB images are integrated to extract these candidates' colours and determine their confidence levels based on whether they are characterized by offshore gas flaring.

2.2.1. Preprocessing of GLI images

Given the vast expanse of sea surface yielding low signals, the GLI Pan band images over open waters tend to exhibit homogeneity. We treated the sea surface as an underlying background and removed residual noise through morphological processing (Wang et al. 2023). Subsequently, regions corresponding to land and islands were masked out from the GLI imagery.
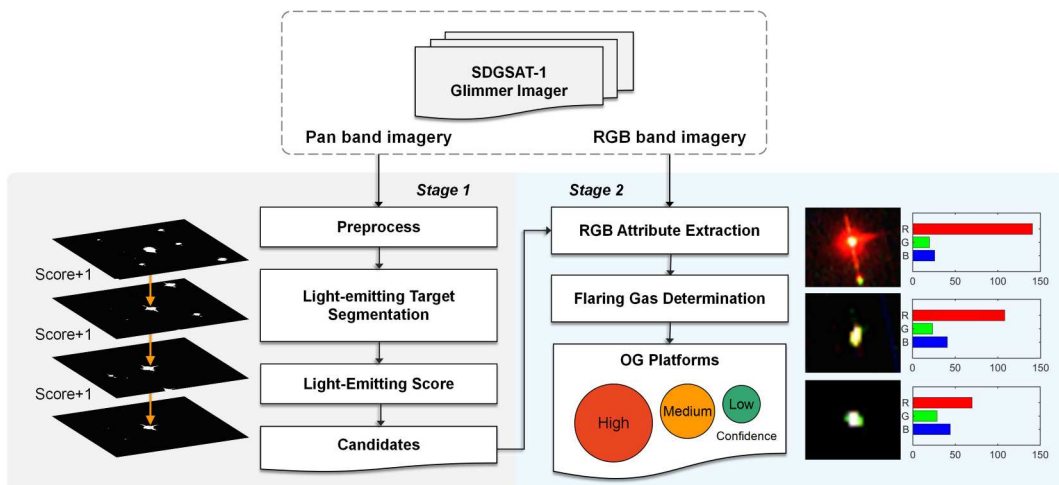
Figure 3. Framework for the offshore OG platform detection by SDGSAT-1 GLI.

2.2.2. Light-emitting target segmentation

We computed the radiance of glimmering pixels from 15 GLI images captured under varying lighting scenarios and conducted iterative threshold tests between 70 and 120 nW/cm^2/sr/µm with a step size of 1. The optimal threshold was determined to be 90 nW/cm^2/sr/µm, resulting in effective binary segmentation. Pixels with Pan-band radiance above this threshold are marked as 1, while those below are labelled 0.

2.2.3. Scoring of targets emitting light

One characteristic that distinguishes offshore OG platforms from light-emitting vessels is their invariant position nature. Capitalizing on this property, we developed a scoring method to quantify the light-emitting frequency for each extracted target by accumulating multi-temporal GLI images. As illustrated in the left panel of Stage 1 in Figure 3, only invariant-position targets were scored in the multi-temporal GLI data. The scoring process employs a traversal lookup. During each lookup, the distance between the two targets is calculated. If the distance is less than the offset threshold, we consider the two targets to correspond to the same entity at an invariant position. If an element corresponding to the same position exists in the table, the light-emitting score assigned to that element is incremented by one point. Elements in the well-established lookup table that achieve scores greater than two points are recognized as platform candidates.

2.2.4. Gas flaring determination

The first stage described above utilized GLI Pan band imagery, specifically tailored to eliminate mobile targets. However, the monochromatic nature of the Pan band provided limited information. Drawing inspiration from the newly designed GLI colour bands, we employed these bands in the second stage to further visualize the light colour emitted from the platform candidates. We re-matched candidate positions in the RGB data using the geographic information recorded from the Pan band data. For each candidate, we extracted its RGB radiance attributes across multiple observations and generated corresponding colour sub-images (with the three channels using GLI R-, G-, and B-band radiance).

As shown in the right panel of Stage 2 in Figure 3, the platform candidates display different colours in those RGB images. Our analysis reveals that candidates exhibiting large clusters of reddish starbursts are active OG platforms engaged in associated gas flaring. This feature significantly distinguishes them from other candidates that emit yellow or cooler hue. Such colour variation reflects the relative energy differences between the R band and the other two bands. Through visual interpretation, we carefully selected 150 samples, including 50 from each of three categories: those emitting clusters of reddish flames, warm yellow light, and cold light. We tested three radiation metrics, R-G, R-B, and 2R-(G + B), and calculated the standardized Euclidean distance (noted as D) between different samples using Equation (2). As shown in the statistics listed in Table 2, the metric of radiance difference between the R and G bands (i.e. R-G) yielded the largest distance of 3.46 across the three classes, demonstrating the best performance in distinguishing different types based on their RGB attributes.

$$D = \frac{|\mu_1 - \mu_2|}{\sqrt{\sigma_1^2 + \sigma_2^2}} \tag{2}$$

Table 2. Statistics of three classes of GLI RGB samples.

Radiance (nW/cm^2 /sr/µm)	Cold-light sample			Warm-light sample			Reddish-light sample			D
	Min	Mean	Max	Min	Mean	Max	Min	Mean	Max	
R − G	−30.37	14.83	24.85	31.01	61.74	84.63	95.42	192.23	256.25	3.46
R − B	−104.82	7.16	53.60	8.06	62.52	112.99	65.31	200.03	272.24	2.52
2R − (G + B)	−119.23	21.99	78.38	47.37	124.26	194.31	161.93	392.26	515.00	3.02
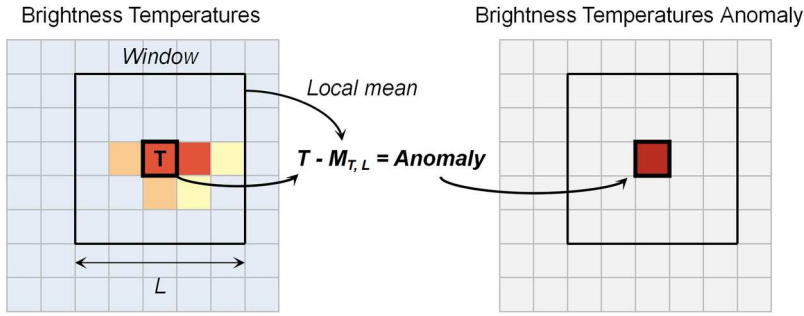
Figure 4. The method for calculating temperature anomaly. The pixel temperature, T, is treated as the centre, while the local mean temperature within a window of length L is extracted, denoted as $M_{T, L}$. The anomaly is calculated by subtracting $M_{T, L}$ from T, i.e. $T - M_{T, L}$.

where $n = 1,2,3$ represents the sample class, μ represents the sample's mean radiance, and σ^2 represents the variance.

Thus, we utilized the R-G radiance difference to gauge their characteristics. The maximum value of the cold-light sample (about 25) and the minimum value of the reddish-light sample (about 95) were established as thresholds to categorize all platform candidates into three confidence levels: low, medium, and high. Considering potential intermittent flaring activities, the highest confidence level across multiple observations from the same platform was retained. The specific criteria are as follows:

1. Low-confidence platforms have an R-G radiance difference < 25, exhibiting cold light.
2. Medium-confidence platforms have an R-G radiance difference between 25 and 85, exhibiting warm yellow light.
3. High-confidence platforms have an R-G radiance difference > 85, exhibiting significant reddish light.

### 2.3. Method of extracting thermal anomaly by SDGSAT-1 TIS

We used the brightness temperatures from the TIS three bands. The temperature anomaly was calculated to highlight the temperature contrast between offshore OG platforms and the surrounding sea surface (Qiu, Li, and Guo 2023). As illustrated in Figure 4, the anomaly represents the difference between a pixel's temperature and the local mean within a specified window. In 30 m resolution TIS images, offshore platforms typically appear as high-temperature targets ranging from 3 to 15 pixels in length. To preserve their gradient features, we selected a window length of 80 pixels.

3. Results

3.1. Synergic observations by the GLI and TIS

The SCS is not only rich in offshore oil and gas (OG) reserves but also serves as a vital maritime trade route, a key part of the Maritime Silk Road. Consequently, numerous light-emitting vessels populate these waters at night, complicating the observation of offshore OG platforms from space, as depicted in the nighttime scene of Figure 1(f).

Initially, by using cumulative scoring from multi-temporal GLI Pan-band data, we excluded mobile light-emitting vessels, identifying 1623 platform candidates in the SCS. These platforms are represented by dots in Figure 5(a), with colours transitioning from green to red to indicate varying light-emitting frequencies. However, relying solely on light-emitting frequency did not
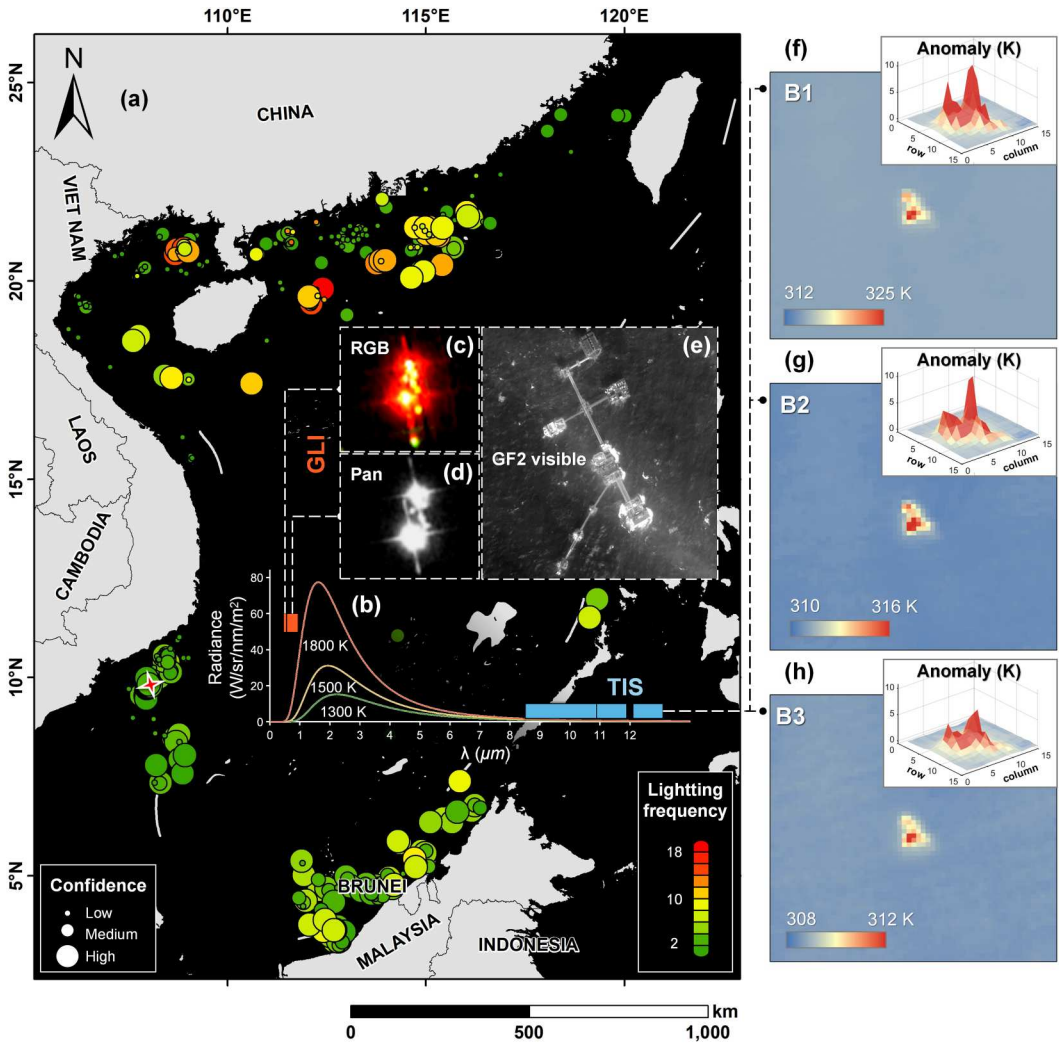
Figure 5. SDGSAT-1 detected OG platforms in the SCS. (a) Pinpointed candidates using GLI data, represented by dots, whose colour indicates light-emitting frequency and size reflects confidence level. (b) Radiometric characteristic curves of simulated flares at 1300, 1500 K, and 1800 K, along with the spectral regions of the SDGSAT-1 GLI and TIS (highlighted by orange and blue boxes). (c) and (d) Observations of an active OG platform featuring two flares captured by the GLI. (e) GF2 visible image used as a reference. (f)–(h) Temperature maps and thermal anomaly profiles of the flares observed by the TIS. The instances shown in (c–h), acquired on February 28, 2022, are the same OG platform, marked by a four-angle star in (a).

definitively categorize a platform as an active OG platform. For instance, some offshore platforms, such as heliports or quarters platforms, may remain continuously lit at night (Mohamed 2020). Thus, the second stage of our algorithm was tailored to address this challenge. By incorporating GLI RGB attributes to assess the confidence levels of these candidates, we successfully pinpointed 113 high-confidence platforms engaged in gas flaring, represented by the largest dots with high confidence in Figure 5(a). These results are robust upon elaborated validation with high-resolution GF2 visible and Sentinel-1 SAR images. The remaining candidates include 319 medium-confidence and 1191 low-confidence platforms.

Figure 5 (c and d) showcase an active offshore OG platform featuring two gas flaring sites, observable in both the GLI Pan and RGB band images. Benefiting from the improved resolution and the colour-band design of SDGSAT-1 GLI, it effectively discloses two clusters of red starbursts and the

elongated skeleton structure connecting them. This structure aligns well with the morphological features seen in GF2 visible imagery (Figure 5(e)), indicating an OG platform complex with gallery bridges linking various units. The GLI onboard SDGSAT-1 excels at observing and characterizing small offshore targets in great detail.

Concurrently, the synergic observations of SDGSAT-1 GLI and TIS unveil that OG platforms engaged in gas flaring, besides emitting luminous signals in the visible and near-infrared channels, also coincide with high-temperature signatures captured in the thermal infrared channels (see Figure 5(b) for spectral ranges of the GLI and TIS). In the case of the OG platform complex, on 28 February 2022, the SDGSAT-1 GLI and TIS sensors captured images almost simultaneously, with the GLI data (Figure 5(c and d)) acquired at 14:11:36 (UTC) and the TIS data (Figure 5(f–h)) at 14:11:53 (UTC). The thermal infrared bands reveal the flares as significant high-temperature events, exceeding 321, 315, and 310 K with anomalies reaching up to 5 K (highlighted red pixels) in Figure 5(f–h) for TIS B1, B2, and B3, respectively. This interesting phenomenon, the concurrent emission of intense light and heat radiance, is characteristic of OG platforms processing associated natural gas through flaring during crude oil production and refining (Faruolo et al. 2021). Thus, the unique nighttime light-heat synergic sensing capability of SDGSAT-1 overcomes spatial resolution limitations while expanding the spectral sensing range, enabling effective tracking of offshore OG platforms.

3.2. Nighttime light radiance

The offshore OG platforms were categorized into three confidence levels based on the SDGSAT-1 GLI data, allowing us to investigate differences in nighttime light radiance. Figure 6(a) presents histograms of Pan band radiance for low-, medium-, and high-confidence platforms. The low- and medium-confidence platforms exhibit a concentrated distribution of low Pan band radiance. In contrast, the high-confidence platforms exhibit significantly higher Pan band radiance, tending to approach saturation, as indicated by the salmon step diagram concentrated at the trailing edge of the spectral radiance in Figure 6(a). This finding confirms that gas flaring activities emit more intense light in the Pan band compared to standard lighting systems (Sharma et al. 2016).
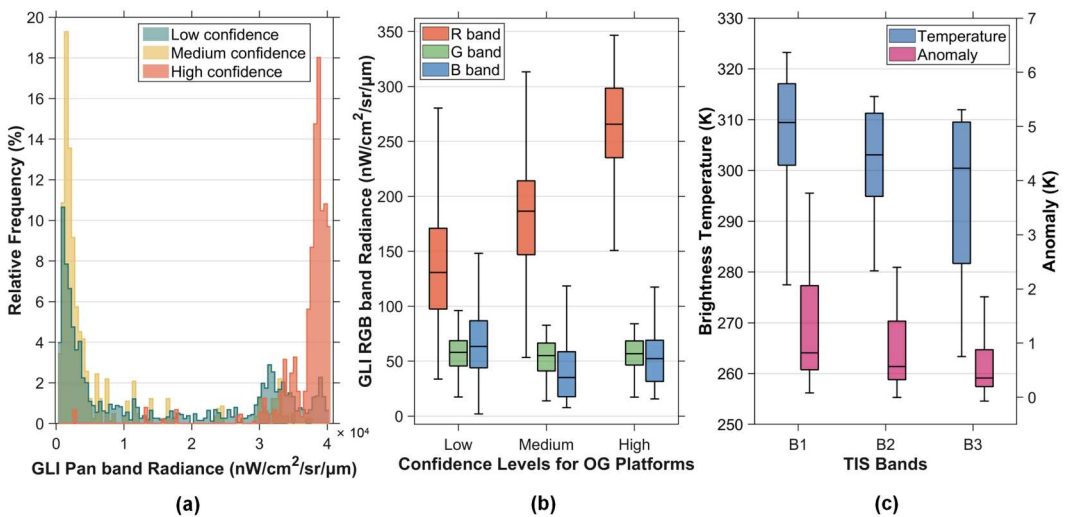
Figure 6. Radiance properties of OG platforms' gas flaring observed by SDGSAT-1 GLI and TIS sensors. (a) Histograms of GLI Pan band radiance for OG platforms with low, medium, and high confidences. (b) Boxplots displaying radiance values in the GLI RGB bands for platforms across the three categories. (c) Boxplots of thermal infrared temperatures and anomalies in the TIS B1, B2, and B3 bands specifically for high-confidence OG platforms.

However, part of the radiance from high-confidence platforms overlapped with that of low-confidence platforms. This confusion suggests that nighttime Pan-band data alone cannot provide detailed information on the platform functions, despite the detection of offshore artificial facilities.

The visible colour bands of the SDGSAT-1 GLI provide novel information on flaring gas. As shown in Figure 5(b), the simulated spectral curves of industrial flares (typically above 1300 K) indicate that the peak radiation lies in the short- to mid-infrared region, with energy increasing across the visible and near-infrared ranges. Thus, flaring flames emit more energy in the R band compared to the shorter G and B bands, which explains why flares on offshore OG platforms appear as red-highlighted starbursts in GLI RGB bands. In contrast, structures utilizing standard lighting exhibit cooler yellowish hues. This insight led us to incorporate GLI RGB-band data to better evaluate the confidence levels of OG platforms based on the Pan-band detection.

Figure 6(b) illustrates the RGB radiance statistics for the three categories. The radiance in the G and B bands shows minimal variation across the categories; however, a significant discrepancy is noted in the R band. High-confidence platforms produce R-band radiance reaching up to 270 nW/cm^2/sr/μm, significantly higher than the medium-confidence and low-confidence platforms. The averaged R-G band difference reaches its maximum of 190 nW/cm^2/sr/μm for high-confidence levels. Thus, the sensitive R band for industrial flaring, coupled with its good contrast with the other two bands (G and B bands), allows for unique signatures of gas flaring (red starbursts), distinguishing them from platforms without such activities. The application of nighttime visible colour attributes offers a more effective criterion for characterizing offshore OG platform activities.

3.3. Thermal infrared radiance

As illustrated in Figure 5(f–h), the TIS onboard SDGSAT-1, operating synchronously with the GLI, effectively captured high-temperature flaring events on active OG platforms. However, thermal infrared imaging is susceptible to interference from atmospheric conditions, particularly smoke plumes produced from industrial combustion. For example, Figure 7 shows two adjacent OG platforms with gas flaring. The TIS observations capture their high temperatures (marked by white squares in Figure 7(a), corresponding to the two dazzling red starbursts presented in the GLI RGB image in Figure 7(b)) while also revealing long, dark-blue trails wafting northward from the flaring sites at a lower temperature of 314 K. These trails, measuring up to 8 km, result from aerosols in the smoke plume, which strongly absorbed long-wave thermal radiance, appearing as low-temperature trails (Fawole, Cai, and MacKenzie 2016). Similar plume phenomena have been found in Sentinel-2 MSI visible images (Zavala-Araiza et al. 2021), also known as important methane sources (Irakulis-Loitxate et al. 2022). Under such interference, the temperature anomalies observed are not robust, with maximum anomalies of only 2 and 4 K for the two platforms in Figure 7(c) (compared to the anomalies as high as 10 K for TIS B1 in Figure 5(f)).

Consequently, among the 113 high-confidence active OG platforms, only 57 platforms were explicitly observed as emitting high-temperature signals during simultaneous GLI and TIS imaging. Six of the remaining 56 platforms, despite showing high-temperature signals, were not included in our analysis as no GLI data was available on the same day. The absence of high-temperature information for the 50 platforms is due to heavy contamination by unclean atmospheres and thus has been excluded from the observation. The statistics of 57 high-temperature OG platforms are presented in Figure 6(c). Intriguingly, both the temperatures and the anomalies follow a gradual decreasing trend from the B1 band towards the B3 band as the thermal infrared wavelength increases. Flares observed in the B1 band exhibit the highest temperature, averaging 310 K, with anomaly averaging 0.9 K and peaking at 6.5 K. The B2-band temperature averages 302 K with an anomaly averaging 0.6 K, while the B3-band temperature averages 300 K with an anomaly averaging 0.3 K.
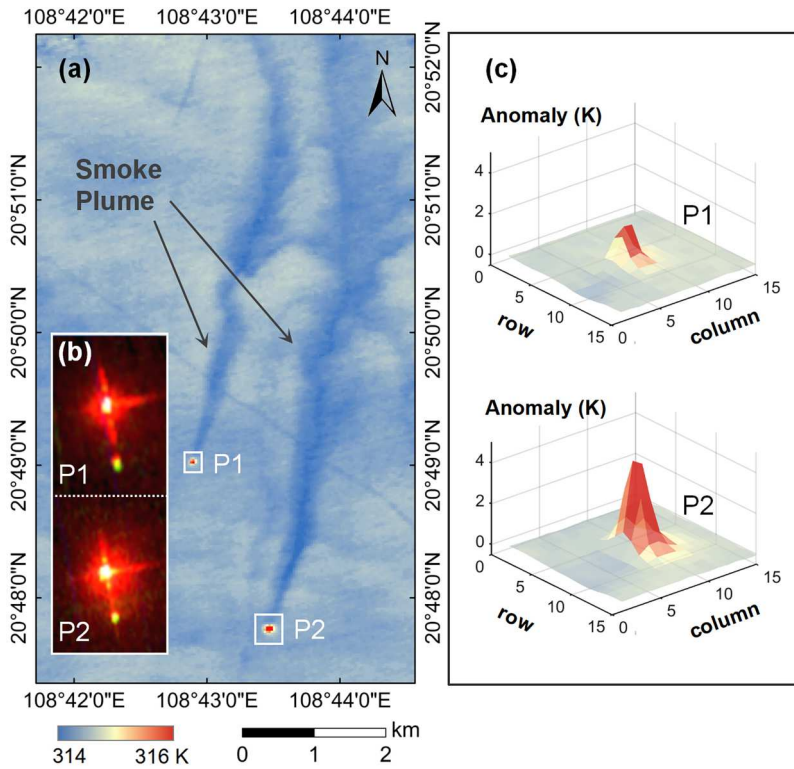
Figure 7. Two cases of active OG platforms with associated gas flaring (P1 and P2) and observed smoke plume by the TIS. (a) Background image showing the TIS B1 temperature map, with two white squares indicating the locations of high-temperature platforms (P1 and P2) and dark gray arrows denoting the low-temperature smoke plume. (b) Co-measured GLI RGB sub-images for the two platforms. (c) Temperature anomaly profiles for the P1 and P2 platforms.

It is surprising to find that the TIS is capable of sensing pronounced high-temperature events, considering thermal infrared channels were not commonly used for observing industrial flares. According to Wayne's displacement law, peak radiation from hotter sources shifts to shorter wavelengths, indicating that industrial flare radiance is typically found in the mid-and short-infrared regions, whereas becomes less pronounced in the thermal infrared region. This is evidenced in Figure 5(b), where the thermal infrared energies (e.g. the blue TIS spectral regions) decrease exponentially compared to the near-infrared (e.g. the orange GLI spectral region) and mid-infrared ranges. Nevertheless, the TIS's good radiometric thermometry performance and high resolution allow it to capture distinct features and flare temperature anomalies. Particularly, the TIS B1 band, with a relatively short wavelength centred at 9.3 μm and a wide channel, is adept at providing supplementary details on the thermal radiation of gas flaring.

3.4 Gas flaring variations

Focused on the pinpointed high-confidence OG platforms, we compiled the correspondence between the GLI-observed light-emitting scores, their colour attributes, and the TIS-observed high-temperature cases (Figure 8). All these OG platforms experienced at least one significant reddish flame detected by the GLI (R-G radiance difference greater than 85 nW/cm^2/sr/μm, shown in dark red in the first few columns of Figure 8). The TIS-observed high-temperature events essentially occur in couples with the GLI-observed prominent red flares, affirming the unique light-thermal characteristics for these 57 OG platforms due to gas flaring.
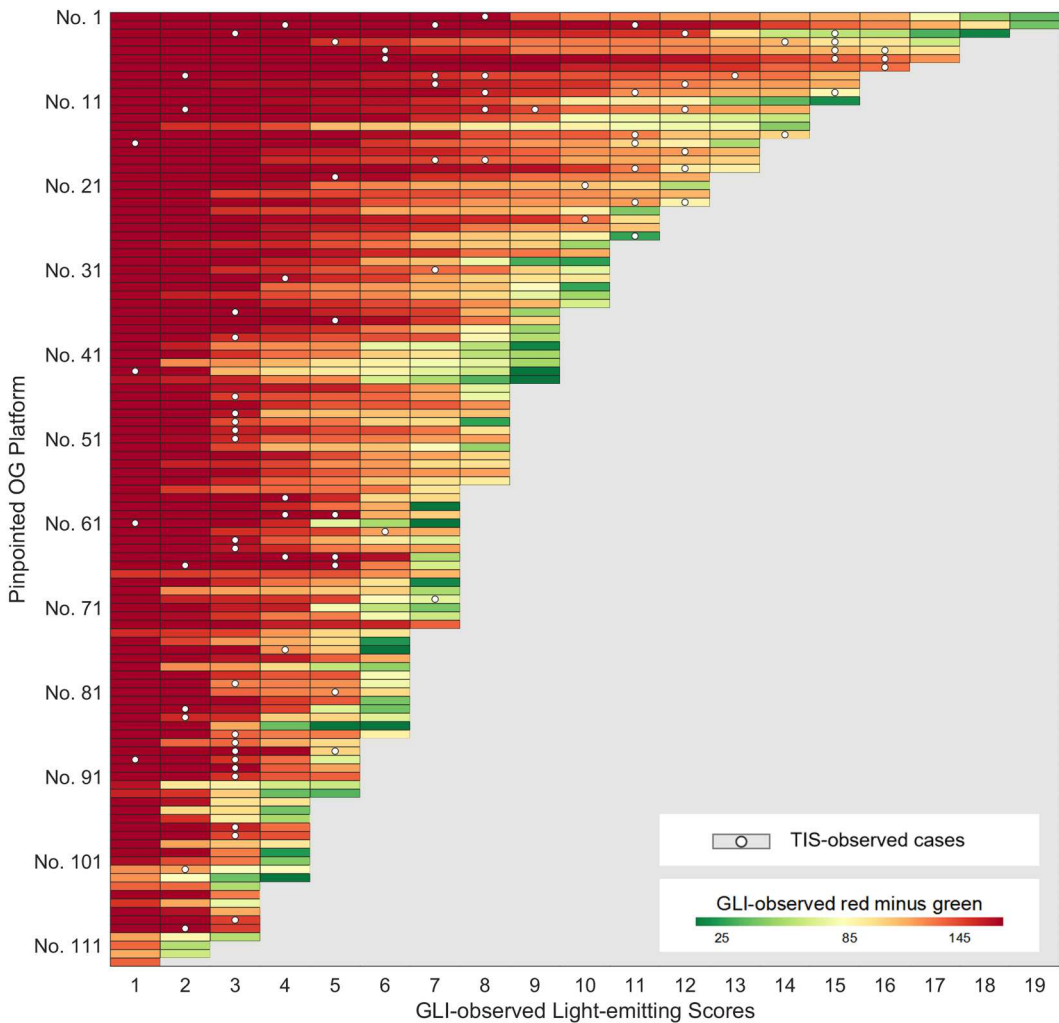
Figure 8. Correlogram between GLI-observed light-emitting scores of high-confidence OG platforms, their colour attributes, and TIS-observed high-temperature cases. The vertical axis (top-to-bottom) lists the 113 high-confidence platforms, sorted by their light-emitting scores in descending order. The horizontal axis indicates the light-emitting frequency scores observed by the GLI with grid colours representing the difference between R- and G-band radiance, also sorted in descending order. White dots mark the high-temperature cases observed by the TIS synchronously.

However, most OG platforms exhibit variable radiance in the GLI R and G bands across different time phases, as shown by these grid colours shifting from red to yellow or even green in Figure 8. Notably, the colour variation is more rapid in cases without TIS observations. Such fluctuations may stem from atmospheric influences on the GLI RGB colours, but they also partly imply intermittent operational changes for these platforms (Faruolo et al. 2021). The time-series mapping of nighttime light colour and thermal information facilitated by SDGSAT-1 offers valuable insights into the operational patterns of OG platforms, enabling effective monitoring of their activities.

4. Discussion

### 4.1. Cross-validation with flaring inventory

We conducted a thorough cross-validation of the offshore OG platforms detected by SDGSAT-1 against available gas flaring datasets, including the VIIRS product and the Sentinel-2 inventory.

Table 3. Comparison results of Sentinel-2 inventory with the SDGSAT-1 high-confidence OG platform in the SCS. Bolds are the case numbers for TP, FN, and FP.

		Sentinel-2 inventory	
		1	0
SDGSAT-1 result	1	True positive: **108**	False positive: **5**
	0	False negative: **43**	True negative: **1467**

As shown in Table 3, our results align well with the Sentinel-2 MSI inventory (Liu et al. 2023), identifying 108 true positives (TPs) represented by orange dots in Figure 9. Upon reviewing the five false positives (FPs), represented by purple dots in Figure 9, we discovered that these platforms did exhibit gas flaring during SDGSAT-1 observations (two even presented high-temperature flares in TIS images) and that their platform entities over sea surface were visible in Sentinel-1 images. However, their relatively smaller size and lower radiance likely caused their omission from the Sentinel-2 MSI.

We also identified 43 false negatives (FNs), marked by blue dots in Figure 9. Investigation reveals that 20 of these FNs correspond to OG platforms with multiple flaring sites. There is a discrepancy in that every flaring site on OG platforms was recorded in Liu et al. (2023) inventory. In contrast, our SDGSAT-1 detection focused on the complete structure of the platform. A good case in point is the two-flare OG platform observed in Figure 5(c and d). SDGSAT-1 captures both flaring starbursts and the connecting bridges efficiently. Additionally, our algorithm employed a positional offset threshold, grouping targets within a distance. Consequently, OG platforms with multiple flaring sites resulted in fewer records in our detection compared to the Sentinel-2 inventory. This discrepancy is reflected by those FNs closely adjacent to some TPs, such as the examples marked with green arrows in Figure 9.
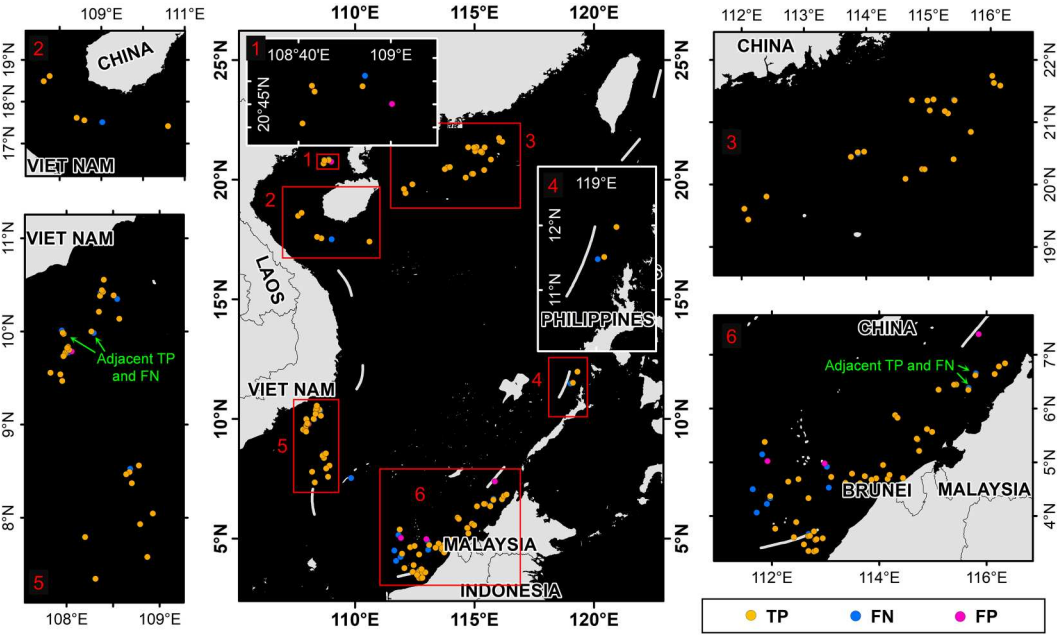
Figure 9. Geographic distribution of the comparisons between the SDGSAT-1 detected OG platforms and the Sentinel-2 inventory (Liu et al. 2023) in the SCS. The large map in the second column provides an overview of the entire study area, with red rectangles marking and numbering six subareas where platforms are densely distributed. Zoomed-in maps of the six subareas correspond to their red numbers of 1–6. Orange, blue, and purple dots in these maps denote the locations of TP, FN, and FP, respectively.

However, after careful checking, the remaining 23 FN results did not show any gas flaring in the SDGSAT-1 data. This discrepancy may arise from different observation periods. The Sentinel-2 inventory (Liu et al. 2023) synthesized the MSI images from 2015 to 2021, whereas the SDGSAT-1 focused primarily on 2022. Thus, some of those aged OG platforms may have undergone reductions in flaring activities or overall human activity. (1) The reduction in gas flaring on OG platforms may result in categorization as low- or medium-confidence in SDGSAT-1 detection. In the Sentinel-2 inventory, we identified 12 lower-confidence platforms with cold lights in the GLI data, and also without high temperatures in the TIS data, possibly reflecting the OG industry's efforts toward the ZRF Initiative and decarbonization. Liu et al. (2023) noted a sustained global decline in gas flaring occurrences from 2016 to 2021 (approximately 6.26%), suggesting that SDGSAT-1's omissions are within reasonable limits. (2) Reduced human activity may indicate platform decommissioning (Sommer et al. 2019). We found 11 Sentinel-2 records without any lights in the GLI data, and also with no identifiable entities in GF2 or Sentinel-1 imagery.

Furthermore, we analyzed the VIIRS active fire and nightfire products. All VIIRS-recorded hotspot events were effectively captured by SDGSAT-1 and included in our high-confidence OG platform category. However, due to the difference in spatial resolution between VIIRS and the GLI and TIS on SDGSAT-1 (hundred-meter vs. ten-meter level), the VIIRS hotspot datasets inevitably miss the information on smaller or closely situated offshore OG platforms. In contrast, SDGSAT-1 proves to be competitive in refining and enhancing existing OG platform inventories.

4.2. SDGSAT-1 GLI and TIS limitations

Although the SDGSAT-1 GLI and TIS sensors demonstrate the potential for observing offshore OG platforms, several limitations still impact their application.

4.2.1. Cloud and atmospheric influence

Cloud cover is a significant factor affecting the availability of remote sensing data. Unfortunately, the bands designed for SDGSAT-1's three payloads do not include a specific band for cirrus clouds detection (1.38 μm), as seen in MODIS band 26 and Landsat 8/9 band 9. It is a major limitation for producing accurate nighttime cloud products. Thus, before the detection, we used the MOD35 product to roughly exclude data with more than 60% cloud cover in the scene. However, it's important to note that there is approximately a 2-hour temporal difference between MODIS and SDGSAT-1, along with significant differences in spatial resolutions. These spatio-temporal mismatches result in the MOD35 product not providing precise cloud information for SDGSAT-1 observations. To mitigate this issue, we further incorporated manual screening aiming to minimize the impact of cloud cover on the GLI and TIS data in this study.

Despite an unclean atmosphere that can affect the nighttime GLI observations, the multi-temporal observations proposed here effectively compensate for possible omissions (or eliminate false alarms) in single-temporal detections, and therefore either the atmosphere or residual clouds have little influence on the GLI data to detect OG platforms. However, applying atmospheric correction to nighttime GLI data could significantly enhance its quantitative applications and is worth exploring in future studies.

4.2.2. GLI and TIS sensors noise

Noise in the GLI and TIS data significantly impacts image quality. In particular, the systematic noise in GLI data can be comparable to artificial lighting. Therefore, it is crucial to remove this noise before application. Our denoising process, adapted from a previous method (Wang et al. 2023), was simplified to account for the homogeneous characteristics of the vast sea surface background, allowing for effective denoising even in complex scenes. For the TIS data, we utilized the L4B data version, which has undergone interstrip denoising, resulting in better image quality.
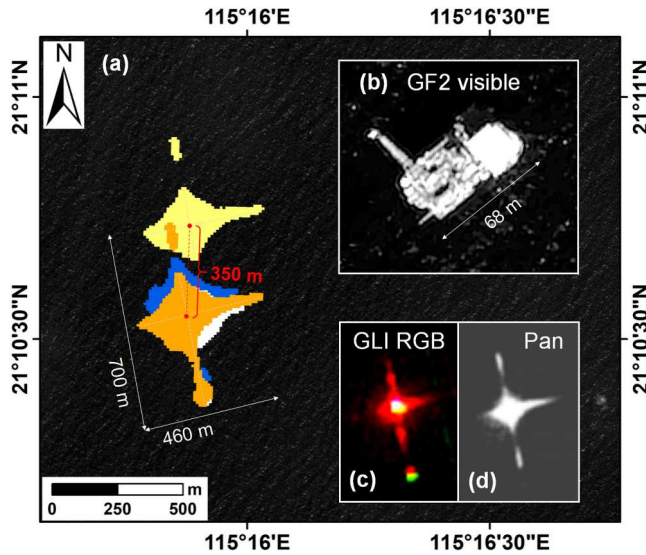
Figure 10. Geolocation offset of SDGSAT-1 GLI data in different time phases. (a) The same OG platforms extracted from the GLI Pan-band data but observed on four different dates: yellow on 24 April, blue on 5 May, orange on 7 March, and white on 31 May. The yellow platform is 350 m off-centre from the others. (b) A reference GF2 visible image, with a long axis of 68 m. (c) and (d) Corresponding sub-images of SDGSAT-1 GLI RGB and Pan band acquired on 7 March.

4.2.3. Geometric calibration accuracy

The geometric calibration accuracy of SDGSAT-1 GLI data is limited at sea. As shown in Figure 10(a), the same OG platforms observed from four time-phase Pan-band data reveal significant geometric offsets, which can differ by up to 350 m. Considering this unavoidable issue, we specifically designed a spatial offset threshold in the first-stage detection of OG platforms, and classified platform candidates within a certain spatial range as the same entity across multiple time phases to overcome the offset caused by inaccurate geolocation. However, this approach limited the GLI detection's ability to discriminate between multiple flaring sites on a single platform, which led to discrepancies with the Sentinel-2 inventory (Section 4.1). Regardless, enhancing the geometric calibration accuracy of SDGSAT-1 data over the ocean remains crucial.

5. Conclusion

The SDGSAT-1 satellite is equipped with GLI and TIS sensors that enable synchronized nighttime observations. This study demonstrates the synergic sensing of the two sensors in not only pinpointing offshore platforms but also, more importantly, understanding their light- and heat-emitting activities. In light of the characteristics of offshore OG platforms, we developed an algorithm based on a combination of GLI Pan and RGB bands to effectively distinguish active offshore OG platforms engaged in associated gas flaring from other artificial facilities. To the best of our knowledge, this is the first study to apply nighttime visible bands for gas flaring observation, highlighting the promise of nighttime GLI RGB imagery for detecting such hotspot events. Simultaneously, the TIS sensor provided clear identification of high-temperature anomalies on OG platforms, confirming the signatures of gas-flaring activities, with the TIS B1 band offering complementary insights into thermal radiation from flares. However, we identified some limitations of the GLI, highlighting the need for reprocessing SDGSAT-1 GLI historical data to improve data quality. In the future, by integrating nighttime GLI and TIS data alongside daytime MII observations from SDGSAT-1, we could comprehensively monitor OG platforms across the global offshore oilfields, aiding in the better refinement of exisiting OG platform inventories.

Acknowledgements

Author contributions

Xiao-Ming Li conceived the idea and designed the research. Yujia Qiu developed the method and conducted the experiments. Lin Yan provided technical guidance. Zhongzhong Chen collected the experimental data. All authors contributed to writing the manuscript.

Disclosure statement

No potential conflict of interest was reported by the author(s).

Funding

Data availability

Data will be made available on request.

ORCID

Yujia Qiu http://orcid.org/0000-0002-0580-3182
Xiao-Ming Li http://orcid.org/0000-0001-5009-5413
Lin Yan http://orcid.org/0000-0002-0733-4703

References

Ackerman, S., P. R. Menzel, and B. Baum Frey. 2015. "MODIS Atmosphere L2 Cloud Mask Product." (dataset), NASA MODIS Adaptive Processing System, Goddard Space Flight Center, USA. Accessed December 1, 2023. https://doi.org/10.5067/MODIS/MOD35_L2.006.

AlixPartners. 2022. "2022 Offshore Oil & Gas Report." Accessed December 1, 2023. https://www.alixpartners.com/insights-impact/insights/offshore-oil-gas-report-2022/.

Anejionu, Obinna C. D. 2019. "Rationale, Historical Developments and Advances in Remote Sensing of Gas Flares." *International Journal of Remote Sensing* 40 (17): 6700–6719. https://doi.org/10.1080/01431161.2019.1590880.

Anejionu, Obinna Chukwubuikem Diony, George Alan Blackburn, and J. Duncan Whyatt. 2014. "Satellite Survey of Gas Flares: Development and Application of a Landsat-based Technique in the Niger Delta." *International Journal of Remote Sensing* 35 (5): 1900–1925. https://doi.org/10.1080/01431161.2013.879351.

Anejionu, Obinna C. D., G. Alan Blackburn, and J. Duncan Whyatt. 2015. "Detecting Gas Flares and Estimating Flaring Volumes at Individual Flow Stations Using MODIS Data." *Remote Sensing of Environment* 158:81–94. https://doi.org/10.1016/j.rse.2014.11.018.

Casadio, Stefano, Olivier Arino, and Danilo Serpe. 2012. "Gas Flaring Monitoring from Space Using the ATSR Instrument Series." *Remote Sensing of Environment* 116:239–249. https://doi.org/10.1016/j.rse.2010.11.022.

Chakraborty, Srija, Tomohiro Oda, Virginia L. Kalb, Zhuosen Wang, and Miguel O. Román. 2023. "Potentially Underestimated Gas Flaring Activities—A New Approach to Detect Combustion Using Machine Learning and NASA's Black Marble Product Suite." *Environmental Research Letters* 18 (3): 035001. https://doi.org/10.1088/1748-9326/acb6a7.

Csiszar, Ivan, Wilfrid Schroeder, Louis Giglio, Evan Ellicott, Krishna P. Vadrevu, Christopher O. Justice, and Brad Wind. 2014. "Active Fires from the Suomi NPP Visible Infrared Imaging Radiometer Suite: Product Status and First Evaluation Results." *Journal of Geophysical Research: Atmospheres* 119 (2): 803–816. https://doi.org/10.1002/2013JD020453.

Elvidge, Christopher D., Mikhail Zhizhin, Kimberly Baugh, Feng-Chi Hsu, and Tilottama Ghosh. 2016. "Methods for Global Survey of Natural Gas Flaring from Visible Infrared Imaging Radiometer Suite Data." *Energies* 9 (1): 14. https://doi.org/10.3390/en9010014.

Elvidge, Christopher D., Mikhail Zhizhin, Feng-Chi Hsu, and Kimberly E. Baugh. 2013. "VIIRS Nightfire: Satellite Pyrometry at Night." *Remote Sensing* 5 (9): 4423–4449. https://doi.org/10.3390/rs5094423.

Elvidge, Christopher D., Daniel Ziskin, Kimberly E. Baugh, Benjamin T. Tuttle, Tilottama Ghosh, Dee W. Pack, Edward H. Erwin, and Mikhail Zhizhin. 2009. "A Fifteen Year Record of Global Natural Gas Flaring Derived from Satellite Data." *Energies* 2 (3): 595–622. https://doi.org/10.3390/en20300595.

Falqueto, L. E., J. A. S. Sá, R. L. Paes, and A. Passaro. 2019. "Oil Rig Recognition Using Convolutional Neural Network on Sentinel-1 SAR Images." *IEEE Geoscience and Remote Sensing Letters* 16 (8): 1329–1333. https://doi.org/10.1109/LGRS.2019.2894845.

Faruolo, M., A. Caseiro, T. Lacava, and J. W. Kaiser. 2021. "Gas Flaring: A Review Focused On its Analysis from Space." *IEEE Geoscience and Remote Sensing Magazine* 9 (1): 258–281. https://doi.org/10.1109/MGRS.2020.3007232.

Fawole, Olusegun G., X. M. Cai, and A. R. MacKenzie. 2016. "Gas Flaring and Resultant air Pollution: A Review Focusing on Black Carbon." *Environmental Pollution* 216:182–197. https://doi.org/10.1016/j.envpol.2016.05.075.

Fisher, Daniel, and Martin J. Wooster. 2019. "Multi-decade Global Gas Flaring Change Inventoried Using the ATSR-1, ATSR-2, AATSR and SLSTR Data Records." *Remote Sensing of Environment* 232:111298. https://doi.org/10.1016/j.rse.2019.111298.

Gao, Junlian, ChengHe Guan, and Bo Zhang. 2022. "Why are Methane Emissions from China's oil & Natural Gas Systems Still Unclear? A Review of Current Bottom-up Inventories." *Science of The Total Environment* 807:151076. https://doi.org/10.1016/j.scitotenv.2021.151076.

GGRP (Global Gas Flaring Reduction Partnership). 2021. "Global Initiative to Reduce Gas Flaring: 'Zero Routine Flaring by 2030'." Accessed August 16, 2023. https://www.worldbank.org/en/programs/zero-routine-flaring-by-2030.

Giglio, Louis, Wilfrid Schroeder, and Christopher O. Justice. 2016. "The Collection 6 MODIS Active Fire Detection Algorithm and Fire Products." *Remote Sensing of Environment* 178:31–41. https://doi.org/10.1016/j.rse.2016.02.054.

Guo, Huadong, Changyong Dou, Hongyu Chen, Jianbo Liu, Bihong Fu, Xiaoming Li, Ziming Zou, and Dong Liang. 2023. "SDGSAT-1: The World's First Scientific Satellite for Sustainable Development Goals." *Science Bulletin* 68 (1): 34–38. https://doi.org/10.1016/j.scib.2022.12.014.

Hu, Yonghong, Xiao-Ming Li, Changyong Dou, Gensuo Jia, Zhuoyue Hu, Anlun Xu, Yongzheng Ren, et al. 2023. "Absolute Radiometric Calibration Evaluation of the Thermal Infrared Spectrometer Onboard SDGSAT-1." *International Journal of Digital Earth* 16 (2): 4493–4512. https://doi.org/10.1080/17538947.2023.2274418.

Hu, Zhuoyue, Xiaoyan Li, Liyuan Li, Xiaofeng Su, Lin Yang, Yong Zhang, Xingjian Hu, et al. 2024. "Wide-swath and High-resolution Whisk-broom Imaging and On-orbit Performance of SDGSAT-1 Thermal Infrared Spectrometer." *Remote Sensing of Environment* 300:113887. https://doi.org/10.1016/j.rse.2023.113887.

Irakulis-Loitxate, Itziar, Javier Gorroño, Daniel Zavala-Araiza, and Luis Guanter. 2022. "Satellites Detect a Methane Ultra-emission Event from an Offshore Platform in the Gulf of Mexico." *Environmental Science & Technology Letters* 9 (6): 520–525. https://doi.org/10.1021/acs.estlett.2c00225.

Levin, Noam, Christopher C. M. Kyba, Qingling Zhang, Alejandro Sánchez de Miguel, Miguel O. Román, Xi Li, Boris A. Portnov, et al. 2020. "Remote Sensing of Night Lights: A Review and an Outlook for the Future." *Remote Sensing of Environment* 237:111443. https://doi.org/10.1016/j.rse.2019.111443.

Liu, Yongxue, Yuling Pu, Xueying Hu, Yanzhu Dong, Wei Wu, Chuanmin Hu, Yuzhong Zhang, and Songhan Wang. 2023. "Global Declines of Offshore gas Flaring Inadequate to Meet the 2030 Goal." *Nature Sustainability* 6 (9): 1095–1102. https://doi.org/10.1038/s41893-023-01125-5.

Liu, Yongxue, Weifeng Zhi, Bihua Xu, Wenxuan Xu, and Wei Wu. 2021. "Detecting High-Temperature Anomalies from Sentinel-2 MSI Images." *ISPRS Journal of Photogrammetry and Remote Sensing* 177:174–193. https://doi.org/10.1016/j.isprsjprs.2021.05.008.

Ma, Jinfeng, Lin Li, Haofan Wang, Yi Du, Junjie Ma, Xiaoli Zhang, and Zhenliang Wang. 2022. "Carbon Capture and Storage: History and the Road Ahead." *Engineering* 14:33–43. https://doi.org/10.1016/j.eng.2021.11.024.

Ma, Rui, Wenzhou Wu, Qi Wang, Na Liu, and Yutong Chang. 2023. "Offshore Hydrocarbon Exploitation Target Extraction Based on Time-series Night Light Remote Sensing Images and Machine Learning Models: A Comparison of Six Machine Learning Algorithms and Their Multi-feature Importance." *Remote Sensing* 15 (7): 1843. https://doi.org/10.3390/rs15071843.

Mansoor, Rehan, and Muhammad Tahir. 2021. "Recent Developments in Natural Gas Flaring Reduction and Reformation to Energy-efficient Fuels: A Review." *Energy & Fuels* 35 (5): 3675–3714. https://doi.org/10.1021/acs.energyfuels.0c04269.

Mohamed, Abdallah El-Reed. 2020. "Introduction to Offshore-structures." In *Offshore Structures: Design, Construction and Maintenance*, edited by Matthew Deans, 1–18. Houston, TX: Gulf Professional Publishing.

NASA FIRMS (Fire Information for Resource Management System). 2024. "VIIRS (NOAA-20/JPSS-1) I Band 375 m Active Fire Product NRT" (dataset). NASA/GSFC. Greenbelt, MD, USA: NASA GES DISC. Accessed June 28, 2023. https://doi.org/10.5067/FIRMS/VIIRS/VJ114IMGT_NRT.002.

Qiu, Yujia, Xiao-Ming Li, and Huadong Guo. 2023. "Spaceborne Thermal Infrared Observations of Arctic Sea Ice Leads at 30 m Resolution." *The Cryosphere* 17 (7): 2829–2849. https://doi.org/10.5194/tc-17-2829-2023.

Schroeder, Wilfrid, Patricia Oliva, Louis Giglio, and Ivan A. Csiszar. 2014. "The New VIIRS 375 m Active Fire Detection Data Product: Algorithm Description and Initial Assessment." *Remote Sensing of Environment* 143:85–96. https://doi.org/10.1016/j.rse.2013.12.008.

Schroeder, Wilfrid, Patricia Oliva, Louis Giglio, Brad Quayle, Eckehard Lorenz, and Fabiano Morelli. 2016. "Active Fire Detection Using Landsat-8/OLI Data." *Remote Sensing of Environment* 185:210–220. https://doi.org/10.1016/j.rse.2015.08.032.

Sharma, Ram C., Ryutaro Tateishi, Keitarou Hara, Saeid Gharechelou, and Kotaro Iizuka. 2016. "Global Mapping of Urban Built-up Areas of Year 2014 by Combining MODIS Multispectral Data with VIIRS Nighttime Light Data." *International Journal of Digital Earth* 9 (10): 1004–1020. https://doi.org/10.1080/17538947.2016.1168879.

Shelestov, Andrii, Andrii Kolotii, Tatiana Borisova, Olena Turos, Gennadi Milinevsky, Igor Gomilko, Tatyana Bulanay, et al. 2020. "Essential Variables for air Quality Estimation." *International Journal of Digital Earth* 13 (2): 278–298. https://doi.org/10.1080/17538947.2019.1620881.

Sommer, Brigitte, Ashley M. Fowler, Peter I. Macreadie, David A. Palandro, Azivy C. Aziz, and David J. Booth. 2019. "Decommissioning of Offshore oil and gas Structures – Environmental Opportunities and Challenges." *Science of the Total Environment* 658:973–981. https://doi.org/10.1016/j.scitotenv.2018.12.193.

Sun, Chao, Yongxue Liu, Saishuai Zhao, and Song Jin. 2020. "Estimating Offshore oil Production Using DMSP-OLS Annual Composites." *ISPRS Journal of Photogrammetry and Remote Sensing* 165:152–171. https://doi.org/10.1016/j.isprsjprs.2020.05.019.

UNCTAD (United Nations Conference On Trade And Development). 2021. "Exploring Space Technologies For Sustainable Development." Accessed August 16, 2023. https://unctad.org/publication/exploring-space-technologies-sustainable-development.

UN (United Nations). 2015. "Transforming Our World: The 2030 Agenda for Sustainable Development." Accessed December 1, 2023. https://sdgs.un.org/publications/transforming-our-world-2030-agenda-sustainable-development-17981.

Wang, Ning, Yonghong Hu, Xiao Ming Li, Chuanli Kang, and Lin Yan. 2023. "AOD Derivation from SDGSAT-1/GLI Dataset in Mega-City Area." *Remote Sensing* 15 (5): 1343. https://doi.org/10.3390/rs15051343.

Wang, Qi, Wenzhou Wu, Fenzhen Su, Han Xiao, Yutong Wu, and Guobiao Yao. 2021. "Offshore Hydrocarbon Exploitation Observations from VIIRS NTL Images: Analyzing the Intensity Changes and Development Trends in the South China Sea from 2012 to 2019." *Remote Sensing* 13 (5): 946. https://doi.org/10.3390/rs13050946.

Wong, Brian A., Christian Thomas, and Patrick Halpin. 2019. "Automating Offshore Infrastructure Extractions Using Synthetic Aperture Radar & Google Earth Engine." *Remote Sensing of Environment* 233:111412. https://doi.org/10.1016/j.rse.2019.111412.

Yan, L., Y. Hu, C. Dou, and X. M. Li. 2024. "Radiometric Calibration of SDGSAT-1 Nighttime Light Payload." *IEEE Transactions on Geoscience and Remote Sensing* 62:1–15. https://doi.org/10.1109/TGRS.2024.3370572.

Yang, Jun, Peng Gong, Rong Fu, Minghua Zhang, Jingming Chen, Shunlin Liang, Bing Xu, Jiancheng Shi, and Robert Dickinson. 2013. "The Role of Satellite Remote Sensing in Climate Change Studies." *Nature Climate Change* 3 (10): 875–883. https://doi.org/10.1038/nclimate1908.

Zavala-Araiza, Daniel, Mark Omara, Ritesh Gautam, Mackenzie L. Smith, Sudhanshu Pandey, Ilse Aben, Victor Almanza-Veloz, et al. 2021. "A Tale of Two Regions: Methane Emissions from Oil and Gas Production in Offshore/Onshore Mexico." *Environmental Research Letters* 16 (2): 024019. https://doi.org/10.1088/1748-9326/abceeb.

Zhizhin, Mikhail, Alexey Matveev, Tilottama Ghosh, Feng-Chi Hsu, Martyn Howells, and Christopher Elvidge. 2021. "Measuring Gas Flaring in Russia with Multispectral VIIRS Nightfire." *Remote Sensing* 13 (16): 3078. https://doi.org/10.3390/rs13163078.